

A Novel 3-D Embedded Module for Displacement Measurement in Metal Structures

David Rojas, *Student Member, IEEE*, and John Barrett, *Senior Member, IEEE*

Abstract—Measurements of relative displacement between the components of structural steel frameworks such as those used in large buildings, bridges, ships, and offshore platforms can be used to detect overstress or impending failure. However, current approaches used to measure displacement require complex arrays of optical sensors or strain gauges. We instead present a novel low-cost wireless 3-D embedded module that uses inductive eddy-current sensing with planar printed circuit board (PCB) coils to measure relative displacement between two or more metal plates. The module is a 50-mm cube with four faces formed by the planar PCB inductors that are used for measurement of relative displacement. The other faces and the hollow center of the cube are used for a four-channel inductive sensing IC, a microcontroller with integrated 802.15.4-compatible radio, antenna, micro-USB serial connector, battery, and battery charger/monitor. The addition of temperature and humidity sensors and a microelectromechanical system inertial measurement unit makes the module into a full structural health monitoring system that can also sense environmental factors, inclination, vibration, and shock. The module was evaluated in two axes in a custom test system that allowed controlled relative movement to two orthogonal mild steel plates, as well as inclination of the plate in a different test setup. The results show that a resolution of 0.5 mm can be achieved in both axes when measuring displacement from the planar coils to the steel plates, with negligible interference between coils/plates on the adjacent faces. The displacement measurement is immune to the presence of water between the planar inductors and the steel plates, allowing the module to be used in applications exposed to high humidity and rain.

Index Terms—3-D module, eddy-current sensor, inductive displacement measurement, structural health monitoring, system in package.

I. INTRODUCTION

STRUCTURAL steelwork forms the skeleton that supports large buildings, bridges, cranes, ships, and marine platforms. Due to structural stresses caused by changes in loading, by environmental changes, and by external stresses from, e.g., seismic or wave forces, the steelwork undergoes cyclic mechanical strain that may cause fatigue and eventual failure [2]. The design of the structure will take this into account as structural movement is unavoidable and movement within

Manuscript received February 10, 2017; revised July 3, 2017; accepted September 1, 2017. This work was supported by the Science Foundation Ireland through The SFI Centre for Marine and Renewable Energy Research (MaREI) under Grant 12/RC/2302 [1]. Recommended for publication by Associate Editor V. Chiriac upon evaluation of reviewers' comments. (*Corresponding author: David Rojas.*)

The authors are with the Nimbus Centre for Embedded Systems Research, Cork Institute of Technology, T12 Y275 Cork, Ireland (e-mail: f.rojas-calvente@mycit.ie; john.barrett@cit.ie).

Color versions of one or more of the figures in this paper are available online at <http://ieeexplore.ieee.org>.

Digital Object Identifier 10.1109/TCPMT.2017.2749278

design limits should not cause failure before design end of life. However, atypical loading or undetected structural deterioration or damage may lead to structural strain and displacement that is outside design limits; this may cause accelerated structural failure. Detecting such atypical displacement is the focus of many structural health monitoring systems (SHMS) [3] that use a network of sensors deployed on the structure. Sensors include foil [4] or fiber-optic strain [5], inclinometer [6], vibration [7], laser [8], radar [9], guided wave [10], impedance [11], and imaging [12]. These sensors typically have one or more of the disadvantages of large size, high power consumption, high cost, ability to measure only externally visible structural components, complexity in measuring movement in more than one dimension/axis, or requirement to embed during construction. SHMS may also look for material deterioration, e.g., cracking or corrosion, using surface or bulk material sensors including strain, guided wave, impedance, acoustic [13], imaging, and eddy-current sensors [14]. Eddy-current sensors use inductive coupling to metal on the principle that metal deterioration will change the coupling between the sensing inductor and the metal. Eddy-current sensors are also widely used for position sensing and gap measurement in rotating machinery [15], [16]. However, in the context of SHMS, eddy-current sensors have been little used for measurement of structural movement. For SHMS, they have the advantage of low sensitivity to dust and humidity in the measurement gap [17]. They have the disadvantage of sensitivity to temperature [18], but this is less of a concern in SHMS where temperature is typically at atmospheric ambient, temperature gradients are small, and temperature variations are slow. Where temperature is a concern, a temperature sensor can be used to allow compensation. Kypris and Markham [19] describe an eddy-current sensor for SHM, but this is focused specifically on monitoring of expansion gaps in concrete structures.

In this paper, we present a miniature low-cost wireless battery-powered cuboid embedded module for structural displacement measurement in multiple axes. It uses planar printed circuit board (PCB) eddy-current coils and commercial off-the-shelf (COTS) inductive measurement ICs to measure relative displacement between up to four adjacent components of a metal structure. This allows it to monitor, for example, structural steel connections where the module is fixed to one beam and used to monitor displacement relative to adjacent beams, as shown in the concept in Fig. 1. The module could also be used on nonsteel structures by simply fixing a small metal plate to an adjacent concrete, wooden, or composite beam. As the sensor module is small and the eddy currents

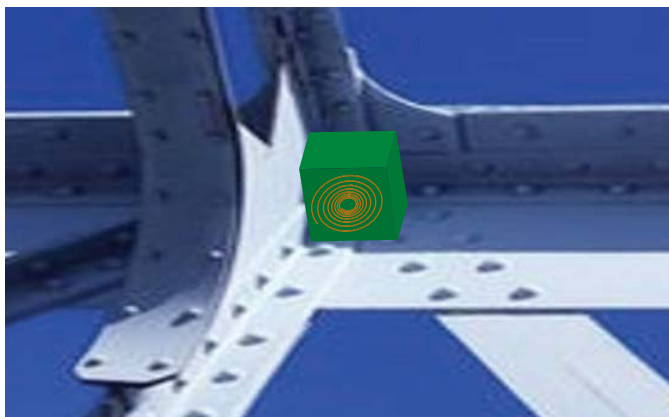


Fig. 1. Conceptual deployment of the module on a structure.

flow only in the surface layer, the plate will be small and thin and have a negligible effect on the displacement of the structure. The module has a 20-mm measurement range with 0.5-mm resolution, values which are typical of those reported in the displacement papers already referenced above. To characterize and calibrate the sensor module, we used a custom test rig that allows controlled relative movement between the module and a metal corner plate. The test rig used laser displacement sensors to measure this relative movement, allowing calibration of the planar sensing coils. As structural deformation may frequently lead to bending (rather than parallel displacement), we designed a second test rig to measure angle of inclination of the target material relative to the sensor. The functionality of the module for SHM is enhanced by the inclusion of an inertial measurement unit (IMU) for vibration/inclination measurement and an environmental monitor (temperature and humidity).

The remainder of this paper presents the concept, design, assembly, testing, and calibration of the sensing module. Section II presents the overall system concept and design. Section III describes the design of the planar inductor eddy-current sensor and interface electronics and calibration of the inductor against laser displacement sensors. Section IV evaluates the performance of the inductive sensors in multiple axes, while Section V presents the electronics (processing, communication, IMU, environmental sensor, and power) and module systems integration. This paper ends with overall conclusions and plans for future work.

II. SYSTEM CONCEPT DESIGN

The system will be a structural monitoring sensor node that is self-contained, wireless, autonomous, and rechargeable. It will measure relative displacement between two or more adjacent metal components in a structural framework and will also measure temperature, humidity, vibration, inclination, and shock. Displacement will be measured by contactless inductive sensing using planar PCB inductors. To measure displacement in multiple axes, the system form factor will be a hollow 50-mm cuboid module formed by PCBs and enclosing the electronics and batteries. The cuboid removes the need for a module casing and allows easier module encapsulation.

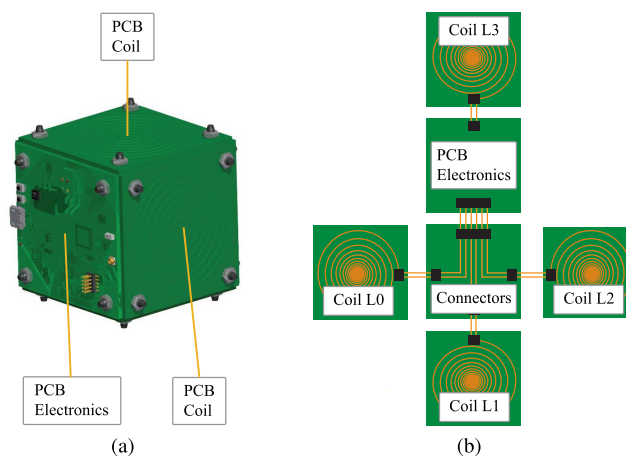


Fig. 2. (a) Cube module concept. (b) Unfolded cube concept.

Mounting fixtures could also be molded into the encapsulation. This paper presents a simple cubic module for proof of concept, but the module could conceivably also be trapezoidal in 3-D, allowing displacement measurement between structural components that are not orthogonal or parallel. Assembly and encapsulation would be more complex but still feasible.

Fig. 2(a) shows a computer-aided design render of the cubic design and Fig. 2(b) shows an unfolded “crucifix” view of the individual PCBs. Four of the faces are planar sensing “COIL” PCBs, three on the “lateral” sides (L0–L2) and one on “top” (L3) allowing relative displacement measurement between up to four structural components. The “CONNECTOR” PCB at the crucifix center acts as a base for inter-PCB connectors and routes the lines from inductors L0–L2 to the “ELECTRONICS” PCB with processing, communications, IMU and T/H sensors, and power. The L3 PCB is connected directly to the “ELECTRONICS” PCB.

We believe that the module cost is lower than existing techniques. It is small and uses low-cost components and PCBs. It involves no specialized, large, or expensive sensors such as strain gauges, mechanical displacement gauges, cameras, or lasers. As it is wireless, it removes the cost of cabling.

III. INDUCTIVE DISPLACEMENT SENSOR DESIGN AND CHARACTERIZATION

A. Sensor Interface Electronics

Nabavi and Nihtianov [18] present detailed design strategies for eddy-current inductive sensor interface electronics, but to reduce size and power consumption and to optimize performance, they have used a COTS IC dedicated to inductive sensing. This is the inductance to digital converter (LDC1614) [20] from TI, a four-channel 28-b LDC, optimized for PCB planar inductors.

The principle of operation is based on the circulating currents, known as eddy currents, induced in a conductive material when it is brought near an ac magnetic field generated by an inductor. The eddy currents generate their own magnetic fields that oppose that of the inductor. This can be viewed as two coupled inductors whose global inductance changes as a function of the size, distance, and/or composition of the target

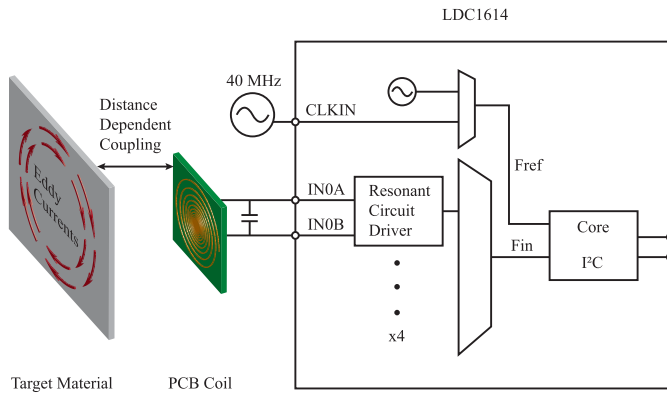


Fig. 3. LDC1614 diagram and eddy-current sensing principle of operation.

material. The LDC1614 generates the ac magnetic field using a resonant circuit driver connected to an LC tank formed by the PCB coil and a parallel capacitor. The inductance changes are measured by comparing the resonant oscillation frequency of the LC tank, given by (1), with an external reference frequency. The digitized sensor data counts read from the sensor, $DATA_x$, represent this ratio $f_{\text{SENSOR}}/f_{\text{REF}}$. The f_{SENSOR} can be calculated from the data counts using (2), and thus the total inductance L from (1). As the size and composition of the target material in SHM remain constant, the measured data counts will represent changes in the distance from the sensing PCB coil to the target. A diagram of the sensor operation and internals of the LDC1614 is in Fig. 3

$$f_{\text{SENSOR}} = \frac{1}{2\pi\sqrt{LC}} \quad (1)$$

$$f_{\text{SENSOR}} = \frac{DATA_x * f_{\text{REF}}}{2^{28}}. \quad (2)$$

B. LC Resonator Design and Characterization

The guidelines in the LDC1614 datasheet [20] and application report [21] set out design parameters for a high Q-factor sensing coil optimized for use with the IC. The sensor resolution is best out to a range of approximately the radius of the sensing coil. Sensing is possible beyond that range, but the resolution is less. As our aim is for a 0–20-mm sensing range, we therefore need a PCB coil of 35–40-mm diameter. The TI guidelines recommend an inductor inner-to-outer diameter ratio of $D_{\text{in}}/D_{\text{out}} > 0.3$ to maintain a high Q-factor.

A standard PCB size of 50×50 mm allows an inductor outer diameter D_{out} of 38 mm while providing enough space for the connector and assembly bolt holes. An internal coil diameter of 12 mm gives a $D_{\text{in}}/D_{\text{out}}$ value of 0.32. The coil design is two layers, 6-mil track width, and 6-mil track gap as this is the minimum track/width size available from the PCB supplier that also maximizes the quality factor (see calculations below). Fig. 4(a) shows the planar PCB coil with a two-pin connector at the bottom and a mounting hole in each corner.

The inductance and quality factor can be calculated with either of the two tools supplied by TI, an offline Excel sheet [22] or the online Web WEBENCH tool [23], based on finite element modeling and simulations. These tools also provide the value of the external capacitor

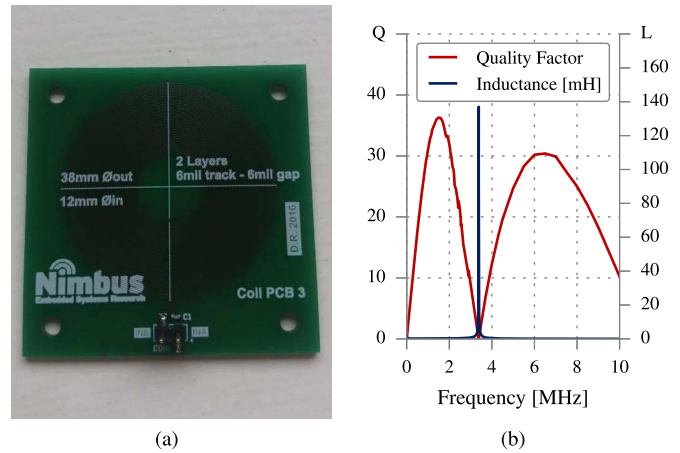


Fig. 4. (a) PCB coil. (b) Measurements of inductance and quality factor of the PCB coil using an impedance analyzer.

for setting the sensor operating frequency and the self-resonant frequency and resistive component of the coil. Although the sensor can work from 1 kHz to 10 MHz, to achieve the best resolution, TI recommends a ratio of $f_{\text{SENSOR}}/f_{\text{REF}} = 0.025$ and $f_{\text{SENSOR}} < 0.8 * f_{\text{SR}}$. Since f_{REF} comes from an external 40-MHz crystal oscillator, f_{SENSOR} is about 1 MHz. The inductance for the 38-mm coil, using WEBENCH, is $L = 139.7 \mu\text{H}$, with $Q = 36.61$ and self-resonant frequency $f_{\text{SR}} = 6.731$ MHz. With an external capacitor $C = 120$ pF, the working frequency of the LC resonator is $f_{\text{SENSOR}} = 1.209$ MHz, well below f_{SR} . A higher coil PCB layer count would have significantly increased the inductance and, to keep the optimal f_{SENSOR} , the value of C would have had to be lower, falling below the recommended specifications.

Although the TI design tools allow a quick design of the sensing coil, the calculated coil parameters are based on an ideal planar inductor. The tools do not take into account the influence of connectors, connecting tracks, through holes, and variations in line/space dimensions or dielectric thickness due to manufacturing. We therefore measured the inductors using an HP-4192A impedance analyzer with a 10 kHz–10 MHz sweep. Fig. 4(b) shows that higher quality factor was found between 1 and 2 MHz, while the inductance peak at 3.1 MHz indicates the self-resonant frequency, half of the design tool predicted value. With $C = 120$ pF, the measured inductance at 1 MHz is $L = 185 \mu\text{H}$ with $Q = 31$ and $f_{\text{SENSOR}} = 1.068$ MHz, close to the recommended 1 MHz and still well below the measured self-resonance.

The LC tank circuit is not ideal and has a resistive component R_p , which is also a function of the target distance. The output current of the sensor I_{DRIVE} needs to be set to a value that allows to maintain a constant oscillation amplitude for the minimum R_p value. As the minimum measured value is $R_p = 36.9 \text{ K}\Omega$, the optimal sensor current calculated is $I_{\text{DRIVE}} = 40 \mu\text{A}$ for each coil.

C. Test System Design

To simulate metal displacement, we made an L-shaped metal corner plate that was fixed in place, and we then moved the sensing coils relative to the plate using a reconfigured

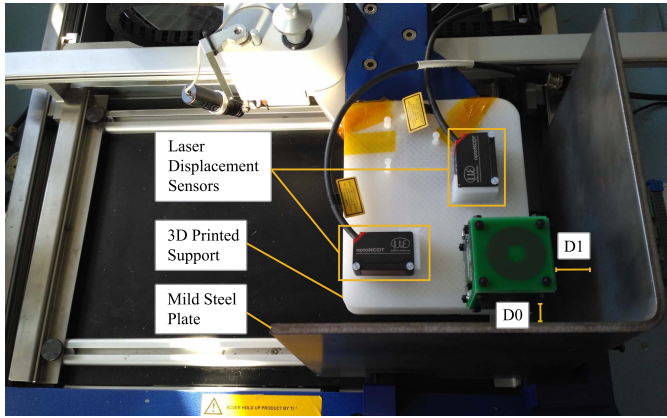


Fig. 5. Test system setup, composed of a retrofitted pick-and-place machine with 3-D printed support parts and laser displacement sensors.

pick-and-place machine (Fig. 5). This allows characterization of the sensors in two axes and investigation of possibly cross coupling or interference between two adjacent metal plates.

In Fig. 5, we can see the test system designed for characterizing the sensor in one or two out of the four possible axes, based on a retrofitted manual pick-and-place machine with several 3-D printed plastic components to fix the metal plate to the machine, as well as a base support to hold the sensing coils. This base is attached to the X–Y moving part of the pick-and-place allowing location and locking of the sensor at any desired distance D from each plate side. Two optoNCDT-142 [24] laser displacement sensors, mounted on the same base plate and pointing in the same direction as the sensing coils, are set 25 mm back from the front face of the coil as can be seen in Fig. 5. This is due to the laser sensors needing a minimum distance of 25 mm to the target. The full range of the sensors is 25 mm, with a linearity of 20–25 μm and a repeatability of 1 μm , more than sufficient to characterize the sensors. The sensors are connected (using the module interface electronics; see Section V-A) to a laptop for data collection.

D. Characterization of the Planar Inductor Sensor

1) *Experimental Setup*: To characterize the inductive sensor, we used a single planar PCB coil to measure distances from 0–20 mm at 1-, 0.5-, and 0.1-mm steps to 20 \times 20 cm mild steel plates of four thicknesses of 4, 6, 8, and 10 mm. There were three different step sizes, first to observe the general behavior of the sensor (1 mm), then to confirm that it can resolve the necessary 0.5 mm observed in the literature, and finally to test if it could resolve a higher resolution (0.1 mm). The four metal thicknesses allowed investigation of the effect of the material thickness in the measurements as described in Section IV-A2.

The LDC1614 IC was configured with the parameters calculated with the WEBENCH tool for the designed coils. The reference count register limits the resolution of the sensor, and is inversely proportional to its maximum sample rate. As the samples were collected manually one by one, a high sample rate was not necessary, and we selected the maximum resolution possible by setting the reference count register RCOUNT = 0 \times FFFF, limiting the maximum sample rate

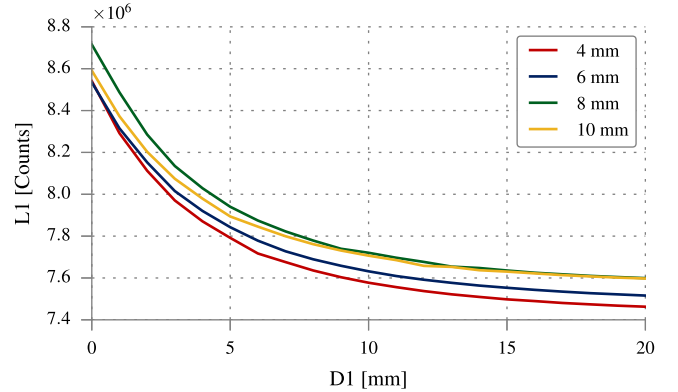


Fig. 6. L_1 counts versus D_1 distance for the different plates, at $D_0 = 20$ mm, with measurements done at 1-mm step.

to 9.5 S/s. This can be changed for different applications up to a maximum of 4.08 kS/s, allowing a theoretical vibration detection bandwidth of 2 kHz. In SHMS, the sampling rate can be slow, and at long intervals, the rate of displacement is typically slow and this will increase battery life. The addition of the IMU (see Section V) gives the option of increasing inductive sensing rates if a sudden large displacement, caused, e.g., by structural failure or seismic shock, is detected by the IMU.

2) *Distance Versus Inductance Results*: Fig. 6 shows the sensor data counts (as defined in Section III-A) for the inductor L_1 for the four metal thicknesses over the 0–20-mm range, at 1-mm steps. The distance D_0 is fixed at its farthest (20 mm), to minimize the interaction of this side of the plate with its orthogonal inductor L_1 and therefore avoid interference with the D_1 measurement (parallel plate). There are small differences between the curves for the different plates. However, as this behavior occurred in all of the measurements, we assume they rather correspond to small errors introduced whenever a plate is inserted and the zero from the laser sensors is set again than to an intrinsic effect of plate thickness. In fact, we know that, due to the skin effect [25], most of the induced currents in the target plates will be confined to the surface of the conductor. If we calculate the skin depth for a mild steel plate using (3), at 1-MHz sensor frequency, it is approximately 4.3 μm , which is 1000 times smaller than the thinnest plate used (4 mm). Therefore, for thicker plates, the generated eddy currents and hence the measured inductance would be similar

$$\sigma = \sqrt{\frac{\rho}{\pi f \mu}}. \quad (3)$$

3) *Sensor Resolution*: The precision of the sensor is mainly determined by the reference count configuration and the ratio of the target distance versus the diameter of the coil. Although the theoretical resolution of the sensor can be less than 10 μm for up to 100% distance/coil diameter, the impact of external variables like the test system setup, the manual adjustments, and the laser sensors will lead to a lower resolution.

In Fig. 7, we can see that the measurements taken at 0.5-mm step have the same shape as the ones in Fig. 6, with monotonic decaying exponential curves, showing that a resolution of at least 0.5 mm is achieved. However, in Fig. 8,

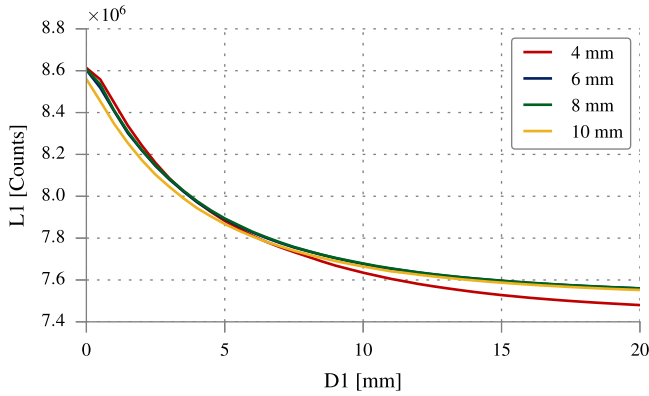


Fig. 7. L_1 counts versus D_1 distance for the different plates, at $D_0 = 20$ mm, with measurements done at 0.5-mm step.

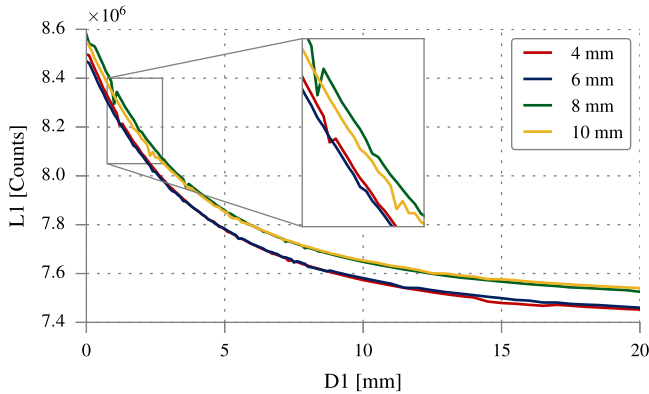


Fig. 8. L_1 counts versus D_1 distance for the different plates, at $D_0 = 20$ mm, with measurements done at 0.1-mm step.

we observe noise when measuring at 0.1-mm step, as the curve is not monotonic in all the points, which indicates that our system setup cannot accurately resolve 0.1-mm increment displacements. Comparing Figs. 6–8, there is a measurement uncertainty of 2 mm. This is not an inherent uncertainty of the measurement method, but happens because of the manual setup of each individual set of measurements. When we insert a metal plate in the system, we must move it until it touches the module screw tops. Then we set the laser sensors to zero at that position. This base position always varies slightly because of the multiple plastic parts in the setup, which bend slightly when tightening up the screws.

The overall conclusion from all of the above measurements is that the sensor module in the current test setup can detect displacement over a 0–20-mm range with at least 0.5-mm resolution. The apparent measurement uncertainty due to the limitations of our existing measurement setup will not affect a real-world measurement as the sensor module will be solidly fixed in place on its base structural member and will be measuring relative movement of an adjacent structural member.

IV. DESIGN AND CHARACTERIZATION OF A MULTIAXIS PLANAR INDUCTOR SENSOR FOR METAL PLATE MOVEMENT MEASUREMENT

A. Characterization of a Planar Inductor Sensor in Two Axes

1) *Experiment Setup:* In the cuboid module, the planar coil PCBs on orthogonal faces are adjacent to each other and

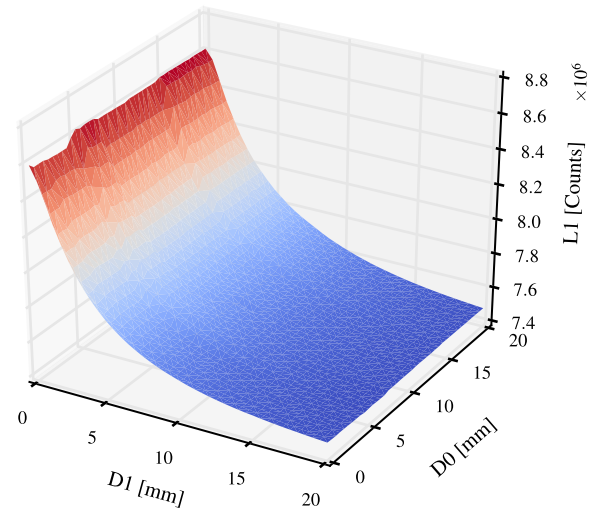


Fig. 9. L_1 counts versus D_1 and D_0 distance for the 4-mm plate, at 0.5-mm step.

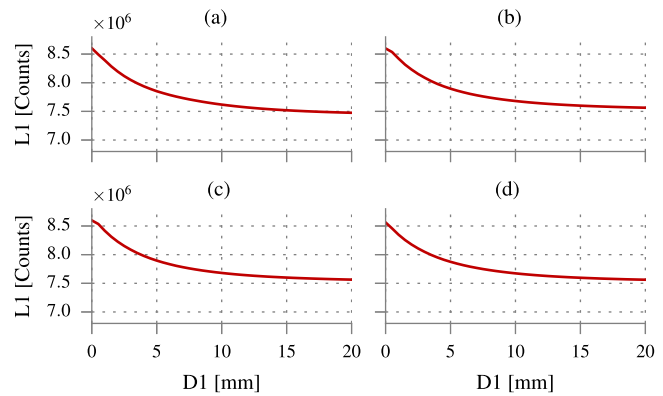


Fig. 10. Average L_1 counts versus D_1 distance curves over the D_0 range for the different plates. (a) 4-mm plate. (b) 6-mm plate. (c) 8-mm plate. (d) 10-mm plate.

face an orthogonal metal L-plate, and cross coupling and interference are possible. To characterize this, we performed a full set of measurements for both of the coil–plate distances D_0 and D_1 , coils L_0 and L_1 , respectively, for the 0–20-mm range, at 0.5-mm steps.

2) *Effect of D_0 Distance on L_1 Inductor:* The effects of the proximity of a plate on its adjacent orthogonal coil are shown in Fig. 9, a 3-D representation of all the curves for L_1 data counts versus D_1 for the whole range of D_0 distances, for the 4-mm-thick plate. We see that the effect is minimal and only when the sensor is closer to the D_0 plate, due to the higher sensitivity of the LDC1614 IC when the coil is closer to the target. The largest standard deviation for this plate is 55308 (0.65% of the maximum value) and occurs when $D_1 = 0$, which is also the maximum found among all the different plates. In Fig. 10, we see the average of these L_1 versus D_1 curves for the D_0 range, for every plate thickness.

Overall, it can be concluded that the presence of even thick metal plates adjacent and orthogonal to a given sensing coil does not have a significant effect on the measurements made using that coil. Both sensors can therefore operate independently with identical performance.

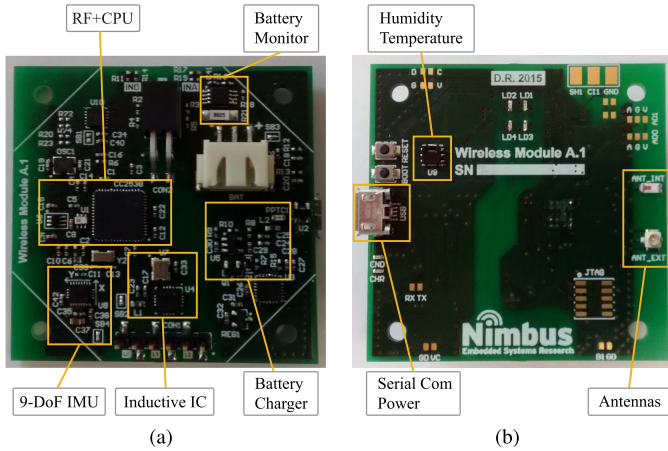


Fig. 11. (a) Top-layer PCB (internal side). (b) Bottom-layer PCB (external side).

V. MODULE SYSTEMS INTEGRATION

The four planar coil PCBs are 50-mm square and, with a cubic module, this means that the other two boards (ELECTRONICS and CONNECTORS) are also 50 mm. Section V-A presents the design of these two boards and Section V-B the firmware developed for the module. Electrical connection between the PCBs is by connectors and mechanical assembly (Section V-C) is by internal plastic corner pieces and bolts. Section V-D describes the battery integration. Finally, Section V-E presents the testing of the module.

A. Main Electronics Board

The ELECTRONICS PCB contains most of its components in the top layer [Fig. 11(a)] facing the inside of the cube, to protect them from the environment and to give some electrical shielding. The core is the CC2538 [26] wireless microcontroller with integrated radio for 2.4-GHz IEEE 802.15.4-based applications. There are three different types of sensors connected to this microcontroller through an I²C bus: an inductive displacement sensor, an LSM9DS1 [27] IMU (three-axis accelerometer, gyroscope, and magnetometer), and an SHT21 [28] humidity/temperature sensor. As low-power operation is important for the application, a DS2745 [29] battery monitor is also on the same I²C bus. For power management, a battery charger IC [30] and a low-dropout regulator [31] are used, providing a stable 3.3 V from the nominal 4.2 V of the battery.

On the opposite, outer face of the PCB [Fig. 11(b)] are the components that need external exposure, such as the humidity/temperature sensor. For battery charging and firmware updating, a micro-USB connector is also on this side of the PCB, serving both functions with the same connector. Finally, opposite this connector is a surface-mount chip antenna, as well as a small U.F.L connector, to allow use of a higher gain external antenna to extend, if necessary, the wireless range or to locate the antenna at a distance if, for example, the module was inside an enclosed metal space.

The module is powered by 2 × 600 mAh rechargeable lithium polymer batteries integrated inside the cube.

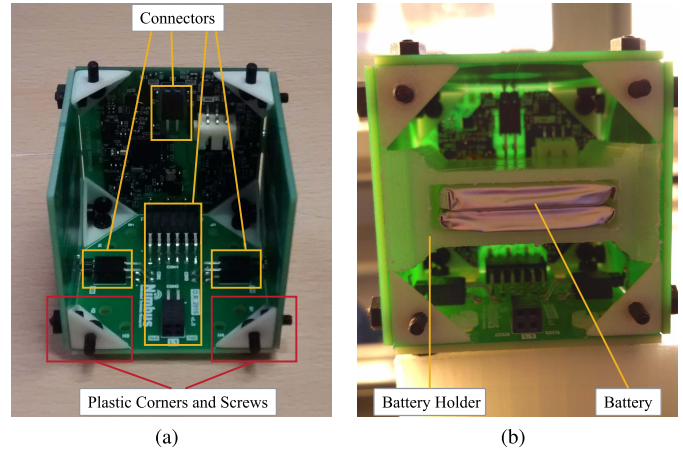


Fig. 12. (a) Module assembly with connectors, plastic corners, and screws. (b) Battery assembly inside the cube.

The power consumption is approximately 25 mA when measuring and 40 mA when transmitting data, with a quiescent current of less than 1 mA when in power down mode. This allows for 50 days of continuous operation if configured to measure and send 1 S/h.

B. Firmware

The firmware developed for the module is built on top of Contiki-OS [32], an open-source operating system for the Internet of things, designed to wirelessly interconnect battery-powered low-cost microcontroller-based devices. Some of its features include support of recent low-power wireless communication standards, such as 6LoWPAN, RPL, and CoAP, which provide full networking capabilities with a low overhead. To allow for remote command execution and sensor configuration, the main application is based on a modified version of Contiki-shell, which makes it easy to extend the platform by adding commands with different functionality. The remote control and data collection is done through a gateway node connected to a laptop, using a custom Python script. The firmware can be updated directly through the micro-USB connector without the need for an external JTAG programmer, due to the embedded bootloader present on the microcontroller.

C. Module Electrical and Mechanical Assembly

To produce a reliable and robust module, its assembly has to be strong enough to withstand handling and deployment, while at the same time providing some flexibility to avoid cracking if the structure to which it is attached bends or vibrates. To minimize interference with the inductive measurements, the materials surrounding the coils and the electronics should be nonconductive, and the assembly therefore uses 3-D-printed plastic parts, nylon screws, and standard 2.54-mm connectors.

Fig. 12(a) shows the internal module assembly. The CONNECTOR PCB at the base of the cube has a horizontal female 2 × 6 pin connector that mates at 90° with the vertical male in the ELECTRONICS PCB, connecting with the differential inputs of the three inductive sensors. Only the



Fig. 13. Fully assembled module in cuboid form, with four PCB faces for planar coils, one for the electronics, and another for internal connectors.

top row of the female connector is used as the bottom row provides the necessary gap for the edges of the two boards to be at the same level. These six lines are then distributed to each of the three PCB coils on the sides through another set of connectors. The top coil is connected directly to a connector on the top of the ELECTRONICS PCB.

To hold the whole module together, a small 3-D printed corner piece is used in every corner, screwed with a 3-mm nylon bolt to each PCB corner, with the nuts facing outside. The corner pieces and the distance between the bolt holes are designed for an interference fit so that, when the bolts are inserted, the assembly holds itself together. In this way, the last side of the cube can be closed and the nuts screwed on from the outside.

D. Battery Integration

A 3-D printed enclosure keeps the battery pack in the center of the cube, as far as possible from the coils and electronics to minimize interference. This enclosure slides in and is held between the 3-D printed corners [Fig. 12(b)].

Fig. 13 shows the assembled cubic module with all integrated sensors and electronics.

E. Module Testing

1) *Test Setup*: As the module is designed to be used as a fully autonomous wireless sensor, most of the test measurements were with the battery inserted in the plastic holder inside the module. However, for very noisy environments, or when wired power is available, a USB connection can be used for communication and power. This would also allow the connection of a larger battery pack to extend battery life or to keep the batteries remote from the module in case of possible interference with the displacement measurements. To test for this possible interference, we compared the module performance with both USB and battery power. As some SHMS applications could involve exposure to high humidity or rain, we also performed a test with water sprayed over one of the inductors, to assess its effects on the measurements.

We have characterized the sensor module for parallel movement of the target material, but structural deformation may also

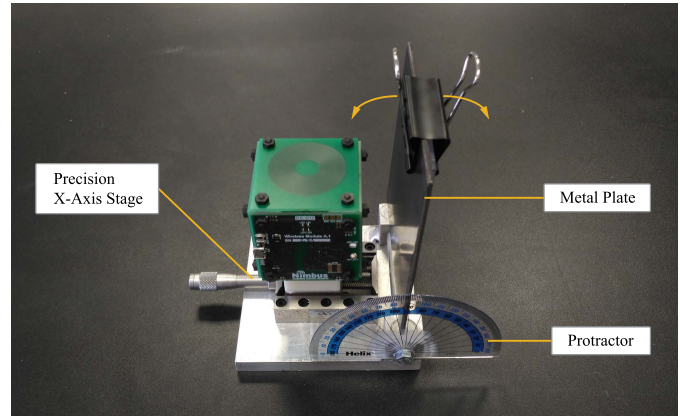


Fig. 14. Test system setup for measuring angle of the plate, composed of a precision x-axis stage and a protractor to measure distance and angle of inclination.

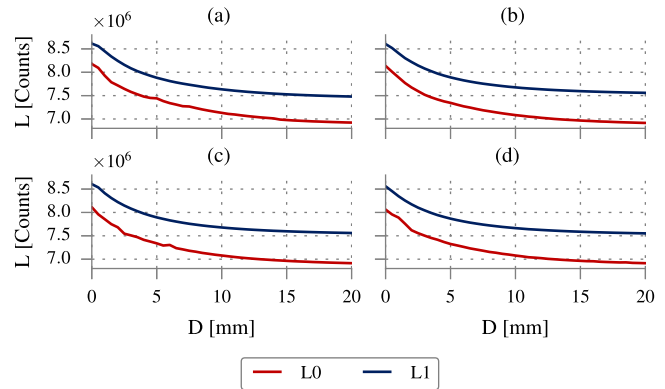


Fig. 15. L counts versus D distance for the different plates, at opposing $D = 20$ mm. (a) 4-mm plate. (b) 6-mm plate. (c) 8-mm plate. (d) 10-mm plate.

involve bending or torsion. To simulate bending, we designed a second test setup (Fig. 14), where we can change the inclination of a metal plate in one axis by a specified angle relative to the sensing coil. While most civil structures are made of steel, we also used this test rig for single axis parallel displacement of other metals. The results from these measurements are given later in this section.

2) *Module Performance*: The fully assembled module performed as expected, with no packet data loss while sampling and transmitting. The temperature sensor recorded a minimum temperature of 24 °C and a maximum of 32.2 °C during the tests. The data from the humidity sensor and IMU were also successfully collected. Fig. 15 represents the curves for $L0$ and $L1$ versus the distance to their corresponding plates, when the distance to its opposing plate is at $D = 20$ mm. On average, $L1$ exhibits a higher L count (lower inductance). This is most likely due to the battery not being square, and then being closer to the $L1$ inductor than to $L0$. The battery covering is partly metallic, and a small eddy-current is induced in the surface of the battery, lowering the total measured inductance. Although this will not have any effect on the accuracy, the offset will have to be taken into account when developing a model for the application.

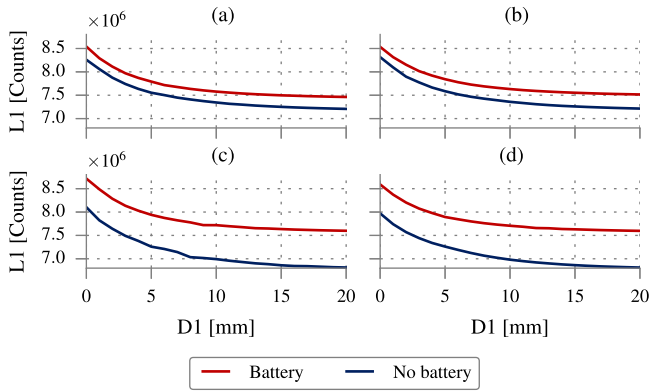


Fig. 16. Effects of the battery integration on the $L1$ counts. (a) 4-mm plate. (b) 6-mm plate. (c) 8-mm plate. (d) 10-mm plate.

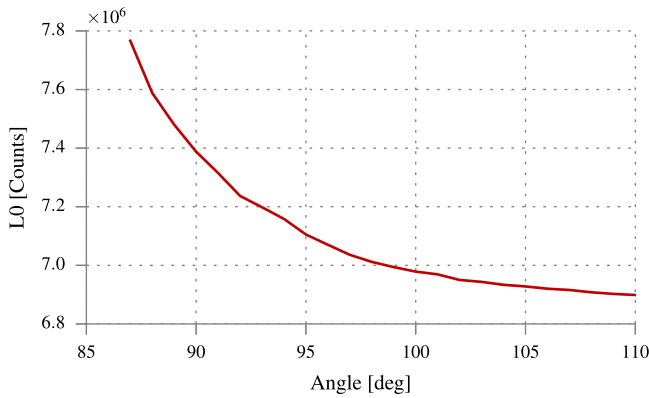


Fig. 17. $L0$ counts versus angle of inclination, at $D0 = 10$ mm.

3) *Effects of the Battery and Water*: Fig. 16 confirms that having the battery inserted instead of the module being powered through USB causes an increase in the $L1$ counts, which corresponds to a decrease in the measured inductance.

The experiments done when water was splashed over the metal did not produce any significant variation in the results compared with the experiments with the dry plates. This test was done first with the dry plates and immediately after was repeated with water splashed, without removing the plates or the sensor nor recalibrating the laser sensors; therefore, the curves of both experiments overlap. This also demonstrates that changes in ambient humidity have a negligible effect on the sensor measurements. Temperature changes will have a bigger effect, but temperature compensation is possible following the guidelines in the sensor IC application report [33].

4) *L Sensor Measurements Versus Plate Inclination*: To show the module's ability to measure plate bending or inclination, we placed a 2-mm mild steel plate parallel at 10 mm from the measuring coil in the test setup of Fig. 14. We changed the plate inclination 87° – 110° relative to the measuring coil, in 1° steps with the results in Fig. 17. This shows that the sensor can measure these changes, demonstrating a similar exponential curve as we observed with parallel plate movement. If detection of torsion of a plate in three dimensions is necessary, a PCB sensing coil could conceivably be designed to use multiple smaller coils on a single PCB; in this way,

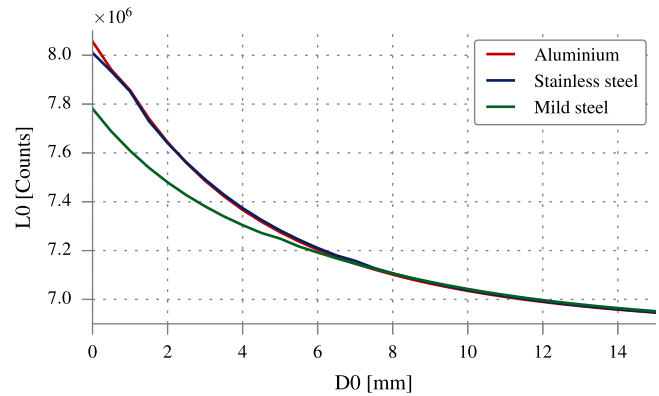


Fig. 18. $L0$ counts versus different metal materials.

a finer movement detection would be achieved. However, the module is primarily intended to detect anomalous structural movements from a baseline. However, these movements are caused, and the measurements in this paper show that it can do this.

5) *L Sensor Measurements Versus Different Metal Materials*: As described in [34], different target materials can affect the measurements due to the differences in their conductivity. Fig. 18 shows the measurements for three different metals: aluminum, stainless steel, and mild steel. Aluminum and this particular alloy of stainless steel have a very similar conductivity; therefore, they present almost identical curves, while mild steel differs. However, it is easy to compensate for these different conductivities by doing initial baseline measurements after sensor module installation on a structure.

VI. CONCLUSION

3-D systems integration and miniaturization techniques have allowed development of a multiaxial metal displacement sensing module and the integration of other sensors along with processing, communications, and power to make a complete standalone wireless SHM module. The eddy-current sensing coil interface IC avoids the need for complex interface circuit design and optimization, allowing more straightforward development of eddy-current sensor applications such as the novel structural steel framework displacement measurement presented here.

The work in this paper has verified that, even with relatively simple two-layer planar inductors, the inductive sensing technique can measure relative displacement of up to 20 mm with a resolution better than 0.5 mm, as well as angle of inclination with at least 1° of resolution. Changing the dimensions of the coils would allow different sensing ranges and resolutions, if needed. The module could also be scaled up in size without changing the inductor dimensions, i.e., a small inductor in the center of a large-area PCB—this would retain the original range and resolution but would allow deployment of the module on larger scale metal structures. The work has also demonstrated that sensors orientated to different axes can work without mutual interference even with other metal components in near proximity. The immunity of the inductive sensors to

moisture/water makes them suitable for exposed and marine applications.

In comparison with existing displacement measurement techniques, the 3-D SHM module in this paper is simple and low-cost to deploy, can work for prolonged unattended periods, and can measure in multiple axes without having to use multiple measurement setups. It can also measure displacement directly without the complex postmeasurement calculations required for, e.g., strain gauges.

The testing described here has verified the original concept. Further testing will involve displacement measurements on up to four axes simultaneously and scaling up to deployment on larger scale laboratory test rigs and, with module encapsulation, eventual deployment on real structures. Finally, we plan to investigate 3-D trapezoidal form factors for deployment on nonorthogonal/nonparallel structural components.

REFERENCES

- [1] *MaREI—Centre for Marine and Renewable Energy*. Accessed: Feb. 1, 2017. [Online]. Available: <http://marei.ie/>
- [2] N. E. Dowling, *Mechanical Behavior of Materials*. London, U.K.: Pearson, 2012.
- [3] W. Ostachowicz and A. Güemes, *New Trends in Structural Health Monitoring*, vol. 542. Vienna, Austria: Springer, 2013.
- [4] H. Jo, J.-W. Park, B. Spencer, and H.-J. Jung, "Development of high-sensitivity wireless strain sensor for structural health monitoring," *Smart Struct. Syst.*, vol. 11, no. 5, pp. 477–496, 2013.
- [5] J. Zhang, W. Hong, Y. Tang, C. Yang, G. Wu, and Z. Wu, "Structural health monitoring of a steel stringer bridge with area sensing," *Struct. Infrastruct. Eng.*, vol. 10, no. 8, pp. 1049–1058, 2014.
- [6] D. W. Ha, H. S. Park, S. W. Choi, and Y. Kim, "A wireless MEMS-based inclinometer sensor node for structural health monitoring," *Sensors*, vol. 13, no. 12, pp. 16090–16104, 2013.
- [7] T. Nguyen, T. H. Chan, D. P. Thambiratnam, and L. King, "Development of a cost-effective and flexible vibration DAQ system for long-term continuous structural health monitoring," *Mech. Syst. Signal Process.*, vols. 64–65, pp. 313–324, Dec. 2015.
- [8] X. Chen, M. Khaleghi, I. Dobrev, W. Tie, and C. Furlong, "Structural health monitoring by laser shearography: Experimental and numerical investigations," in *Experimental and Applied Mechanics*, vol. 6. Cham, Switzerland: Springer, 2015, pp. 149–155.
- [9] G. Luzi, M. Crosetto, and C. Gentile, "Radar interferometry as a tool for structural health monitoring: Current situation and perspectives of the technique for the next decade," in *Life-Cycle of Engineering Systems: Emphasis on Sustainable Civil Infrastructure*. Boca Raton, FL, USA: CRC Press, 2016, p. 145.
- [10] M. Mitra and S. Gopalakrishnan, "Guided wave based structural health monitoring: A review," *Smart Mater. Struct.*, vol. 25, no. 5, p. 053001, 2016.
- [11] N. Kaur, S. Bhalla, R. Shanker, and R. Panigrahi, "Experimental evaluation of miniature impedance chip for structural health monitoring of prototype steel/RC structures," *Experim. Techn.*, vol. 40, no. 3, pp. 981–992, 2016.
- [12] Y. Yang and X. B. Yu, "Real time measurement of the dynamic displacement field of a large-scale arch-truss bridge by remote sensing technology," in *Proc. SENSORS*, 2016, pp. 1–3.
- [13] D. Gagar, P. Foote, and P. Irving, "Effects of loading and sample geometry on acoustic emission generation during fatigue crack growth: Implications for structural health monitoring," *Int. J. Fatigue*, vol. 81, pp. 117–127, Dec. 2015.
- [14] S. Jiao, L. Cheng, P. Li, and X. Li, "Study on fatigue crack monitoring of metallic aircraft structure based on attached eddy current sensor," in *Proc. 2nd Int. Conf. Struct. Health Monitor Integr. Manage. (ICSHMIM)*, Nanjing, China, Sep. 24–26, 2014, pp. 223–229.
- [15] K. S. Chana, V. Sridhar, and D. Singh, "The use of eddy current sensors for the measurement of rotor blade tip timing: Development of a new method based on integration," in *Proc. ASME Turbo Expo Turbomach. Tech. Conf. Expo.*, 2016, p. V006T05A019.
- [16] L. Wang, "Stretchable eddy current noncontact gap sensor based on spiral conductive polymer composite," *IEEE/ASME Trans. Mechatronics*, vol. 21, no. 2, pp. 1072–1079, Apr. 2016.
- [17] S. D. Roach, "Designing and building an eddy current position sensor," *Sensors J. Appl. Sens. Technol.*, vol. 15, no. 9, pp. 56–74, 1998.
- [18] M. R. Nabavi and S. N. Nihtianov, "Design strategies for eddy-current displacement sensor systems: Review and recommendations," *IEEE Sensors J.*, vol. 12, no. 12, pp. 3346–3355, Dec. 2012.
- [19] O. Kypris and A. Markham, "3-D displacement measurement for structural health monitoring using low frequency magnetic fields," *IEEE Sensors J.*, vol. 7, no. 4, pp. 1165–1174, Feb. 2017.
- [20] *TI LDC1614 Multi-Channel 28-Bit Inductance to Digital Converter (LDC) for Inductive Sensing*. Accessed: Feb. 1, 2017. [Online]. Available: <http://www.ti.com/lit/ds/symlink/lcdc1614.pdf>
- [21] *TI Application Report—LDC Sensor Design*. Accessed: Feb. 1, 2017. [Online]. Available: <http://www.ti.com/lit/ds/symlink/lcdc1614.pdf>
- [22] *Inductive Sensing Design Calculator Tool for LDC1xxx*. Accessed: Feb. 1, 2017. [Online]. Available: <http://www.ti.com/lit/zip/slyc137>
- [23] *WEBENCH Designer for Inductive Sensing Applications*. Accessed: Feb. 1, 2017. [Online]. Available: <https://webench.ti.com/webench5/lcdc/>
- [24] *Micro-Epsilon optoNCDT 1420—Smart Laser Triangulation Displacement Sensor*. Accessed: Sep. 19, 2017. [Online]. Available: <http://www.micro-epsilon.co.uk/download/products/cat-optoNCDT-en.pdf>
- [25] W. T. Weeks, L. L.-H. Wu, M. F. McAllister, and A. Singh, "Resistive and inductive skin effect in rectangular conductors," *IBM J. Res. Develop.*, vol. 23, no. 6, pp. 652–660, 1979.
- [26] *TI CC2538 A Powerful System-On-Chip for 2.4-GHz IEEE 802.15.4-2006 and ZigBee Applications*. Accessed: Feb. 1, 2017. [Online]. Available: <http://www.ti.com/lit/ds/symlink/cc2538.pdf>
- [27] *iNEMO Inertial Module: 3D Accelerometer, 3D Gyroscope, 3D Magnetometer*. [Online]. Available: <http://www.st.com/resource/en/datasheet/lsm9ds1.pdf>
- [28] *Sensirion SHT21 Digital Humidity and Temperature Sensor*. Accessed: Feb. 1, 2017. [Online]. Available: <https://www.sensirion.com/products/humidity-sensors/humidity-temperature-sensor-sht2x-digital-i2c-accurate/>
- [29] *DS2745 Low-Cost I²C Battery Monitor*. Accessed: Feb. 1, 2017. [Online]. Available: <https://datasheets.maximintegrated.com/en/ds/DS2745.pdf>
- [30] Microchip. *Microchip MCP73831 Miniature Single-Cell, Fully Integrated Li-Ion, Li-Polymer Charge Management Controllers*. Accessed: Feb. 1, 2017. [Online]. Available: <http://ww1.microchip.com/downloads/en/DeviceDoc/20001984g.pdf>
- [31] Microchip. *Microchip MCP1700 Low Quiescent Current LDO*. Accessed: Feb. 1, 2017. [Online]. Available: <http://ww1.microchip.com/downloads/en/DeviceDoc/20001826C.pdf>
- [32] A. Dunkels, O. Schmidt, N. Finne, J. Eriksson, F. Österlind, and N. T. M. Durvy. (2011). *Contiki: An Operating System for the 'Internet of Things'*. [Online]. Available: <http://www.contikios.org>
- [33] *TI Application Report—LDC1000 Temperature Compensation*. Accessed: Feb. 1, 2017. [Online]. Available: <http://www.ti.com/lit/an/snaa212/snaa212.pdf>
- [34] *TI Application Report—LDC Target Design*. Accessed: Feb. 1, 2017. [Online]. Available: <http://www.ti.com/lit/an/snoa957a/snoa957a.pdf>

David Rojas (S'14) is currently pursuing the Ph.D. degree in electronics engineering with the Nimbus Centre for Embedded Systems Research, Cork Institute of Technology, Cork, Ireland.

He is involved in the development of different wireless modules for structure and machine monitoring, as well as characterizing wireless sensor network communications in marine harsh environments. His current research interests include embedded systems, wireless sensor networks, and packaging solutions for electronic sensor devices.

John Barrett (M'82–SM'96) was an Assistant Director with the Tyndall National Institute, University College Cork, Cork, Ireland. He joined the Cork Institute of Technology, Cork, in 1999, as a Lecturer, where he is currently the Head of Academic Studies with the Nimbus Center for Embedded Systems Research. He has been active nationally and internationally in electronic systems integration research for over 30 years. He has supervised more than 40 postgraduate students and composed over 100 publications in his field. His current research interests include packaging, miniaturization, and embedding of smart systems in materials, objects, and structures with a particular emphasis on challenging and harsh application environments.